

Engineering Applications of Computational Fluid Mechanics

ISSN: (Print) (Online) Journal homepage: www.tandfonline.com/journals/tcfm20

Robust optimisation of the streamlined shape of a high-speed train in crosswind conditions

Yeteng Wang, Zhenxu Sun, Shengjun Ju, Dilong Guo & Guowei Yang

To cite this article: Yeteng Wang, Zhenxu Sun, Shengjun Ju, Dilong Guo & Guowei Yang (2023) Robust optimisation of the streamlined shape of a high-speed train in crosswind conditions, *Engineering Applications of Computational Fluid Mechanics*, 17:1, 2234012, DOI: [10.1080/19942060.2023.2234012](https://doi.org/10.1080/19942060.2023.2234012)

To link to this article: <https://doi.org/10.1080/19942060.2023.2234012>



© 2023 The Author(s). Published by Informa UK Limited, trading as Taylor & Francis Group.



Published online: 20 Jul 2023.



Submit your article to this journal [↗](#)



Article views: 436



View related articles [↗](#)



View Crossmark data [↗](#)

Robust optimisation of the streamlined shape of a high-speed train in crosswind conditions

Yeteng Wang^{a,b}, Zhenxu Sun^{a,b}, Shengjun Ju^{a,b}, Dilong Guo^{a,b} and Guowei Yang^{a,b}

^aKey laboratory for Mechanics in Fluid Solid Coupling Systems, Institute of Mechanics, Chinese Academy of Sciences, Beijing, China; ^bUniversity of Chinese Academy of Sciences, Beijing, China

ABSTRACT

Traditional deterministic aerodynamic optimisation cannot consider environmental uncertainty, which may lead to sensitivity issues. The present study proposes a robust design framework for the aerodynamic optimisation of high-speed trains, which accounts for the uncertain wind and its impact on crosswind stability. In this framework, a variance analysis method based on the Non-Intrusive Polynomial Chaos is proposed to determine the deformation area, and a parametric model is subsequently established. The Non-dominated Sorting Genetic Algorithm-II (NSGA-II) is used as the optimiser to minimise the mean and variance of the aerodynamic response. The mean and variance can be quickly predicted by an uncertainty analysis approach combining Monte Carlo simulation and Kriging model. The framework is then applied to the optimisation of a high-speed train under crosswind. The results of the robust optimisation are compared with those of the baseline geometry and deterministic optimisation. The mean and variance of the rolling moment under crosswind are reduced by 2.26% and 3.37% respectively after optimisation, indicating that the performance and robustness are both improved. The proposed framework is effective for the engineering design of high-speed trains and can also provide a reference for the robust design of other aerodynamic shapes.

ARTICLE HISTORY

Received 16 March 2023
Accepted 1 June 2023

KEYWORDS



Railway aerodynamic;
High-speed train; Crosswind;
Robust optimisation; Flow
structures

1. Introduction

The aerodynamic performance of high-speed trains subjected to crosswinds deteriorates sharply, which may increase the risk of overturning derailments. Indeed, many incidents of trains overturning in crosswind conditions have been reported around the world (Andersson et al., 2004). Thus, the running stability of trains subjected to crosswinds is one of the major problems of railway safety and has been widely studied in recent years (Huo et al., 2023; Liu et al., 2022; Tomasini et al., 2016; Yao et al., 2020) through experimental tests or computational fluid dynamics (CFD) methods. While the experimental investigation enables higher confidence in the absolute values of the measured forces, the numerical calculations allow to easily obtain aerodynamic coefficients and more detailed field information, which is very useful to optimal design. By analysing the flow around the train, Cheli et al. (2010) found that the shape of the train's nose has a significant effect on the stability of the train subjected to crosswinds. The three-dimensional vortex, created by the interaction between the flow separated from the vehicle nose, creates a narrow wake that sucks in the flow passing the body along the leeward flank. This

suction is one of the major causes of the rolling moment. Consequently, crosswind stability is an important indicator of train safety and is largely influenced by the shape of the train's nose.

In recent years, the aerodynamic optimisation of the train's nose has attracted a lot of attention. Traditional methods (Raghunathan et al., 2002) are carried out by evaluating and comparing the aerodynamic performance of several pre-designed shapes which relies on the engineer's experience. Currently, new approaches that use intelligent algorithms for automatic optimisation have become increasingly prevalent. As the utilisation of optimisation requires a substantial number of samples, the construction of surrogate models, such as the Kriging model and the Radial Basis Function model, is frequently utilised to minimise the computational cost. The nose shape of the high-speed train has been optimised using intelligent optimisation algorithms and a surrogate model, both in windless (Yao et al., 2015) and crosswind conditions (Krajnovic et al., 2012; Muñoz-Paniagua & García, 2019). However, although there are many applications of aerodynamic shape optimisation for high-speed trains, none of them is robust enough.

CONTACT Zhenxu Sun  sunzhenxu@imech.ac.cn  Key laboratory for Mechanics in Fluid Solid Coupling Systems, Institute of Mechanics, Chinese Academy of Sciences, Beijing, China; University of Chinese Academy of Sciences, Beijing, China

© 2023 The Author(s). Published by Informa UK Limited, trading as Taylor & Francis Group.

This is an Open Access article distributed under the terms of the Creative Commons Attribution-NonCommercial License (<http://creativecommons.org/licenses/by-nc/4.0/>), which permits unrestricted non-commercial use, distribution, and reproduction in any medium, provided the original work is properly cited. The terms on which this article has been published allow the posting of the Accepted Manuscript in a repository by the author(s) or with their consent.

It is important to notice that existing research on high-speed train optimisation seeks the optimal objective value under ideal and deterministic constraints. However, there are uncertainties in the external environment, especially the wind field, during train operations. In the railway field, some studies have been carried out on the unsteady stochastic wind model (Montenegro et al., 2020) such as the discrete gust model and turbulent wind models, to evaluate the crosswind safety. However, the aerodynamic coefficients of the train used in these evaluations were obtained under a single wind speed, which does not consider the changes in aerodynamic coefficients with the external environment. In this paper, the influence of uncertainty of the external environment is taken into account in the design through robust optimisation. A robust optimisation design is a design insensitive to variations (Park et al., 2006). With the development of computer technology, robust optimisation is becoming more widespread in fluid mechanics. Pelletier et al. (2003) and Luckring et al. (2003) have described the sources and classification of uncertainty in computational fluid dynamics. Unfortunately, the authors are not aware of any publication that considers robust optimisation for a high-speed train.

In this study, a robust optimisation approach is proposed to design the nose shape of a high-speed train, taking into account the uncertain nature of crosswinds. The optimisation objective is to reduce both the expectation and variance of the rolling moment on the leading car. In section 2, the numerical method for CFD simulation is presented, which includes details on the simplified geometry model, the computational domain and boundary conditions, the meshing technique, and the solver utilised. The validity of the CFD method is demonstrated through comparisons with wind tunnel experiments. In section 3, the authors propose a convenient framework for the aerodynamic robust optimisation problem. The comparison and analysis of optimisation results are presented in section 4, where the unsteady flow field is also analysed to study the mechanisms responsible for the improvement. Finally, the study concludes with a summary of the key findings and implications in the last section.

2. Computational model

2.1. Geometry model

The current study focuses on optimising the crosswind stability of the CRH380A high-speed train through the design of the nose shape. To this end, a full-scale simplified model of the Chinese CRH380A train is utilised as the baseline geometry in the optimisation design. The

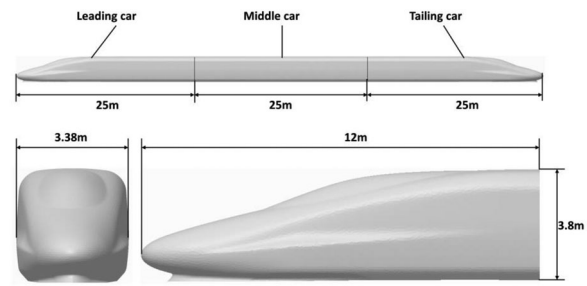


Figure 1. Simplified computational model.

model shown in Figure 1 consists of three cars - a leading car, a middle car and a trailing car, each with a length of 25m. The height of the train models, $H = 3.80$ m, the maximum width, $W = 3.38$ m, and the maximum cross-sectional area, $S = 11.12$ m² remain constant throughout all designs. The leading and trailing cars are identical in shape, with a streamlined nose length of 12 m, whereas the middle car is flat. The aim of this investigation is to solely evaluate the effect of nose shape on crosswind stability. Therefore, the impact of bogies, pantographs and connecting parts is ignored for computational expediency.

2.2. Computational domain, boundary conditions, and meshing

Taking the height of the train, $H = 3.80$ m, as the characteristic length, the computational domain is established, as illustrated in Figure 2. The height of the domain is set at $12H$, a value deemed sufficient to negate the influence of the top boundary. In the longitudinal (X -axis) direction, the distance from Inlet1 to the leading nose is determined to be $10H$, while that from Outlet1 to the tail nose is $20H$. This arrangement can guarantee a fully developed wake. Due to the crosswind conditions, asymmetric positioning is introduced in the lateral direction (Y -axis). The upstream distance is set at $10H$, while the downstream distance is placed at $15H$, which is designed to capture the leeward flow accurately and comprehensively.

Both inlet boundaries of the domain are assigned a velocity inlet condition, while the outlet boundaries are set to zero pressure outlet. The longitudinal velocity of the inlet boundaries is 83.33 m/s, corresponding to the train operation speed, and the lateral velocity is set to vary values to account for crosswind uncertainty. The turbulence intensity is limited to 1% at the inlet. In addition, the no-slip condition is used at both the train surface and the ground surface. The difference is that the ground has a longitudinal velocity of 83.33 m/s while the train is stationary to simulate the real ground effect. Finally, a symmetry boundary is employed at the top of the domain to further.

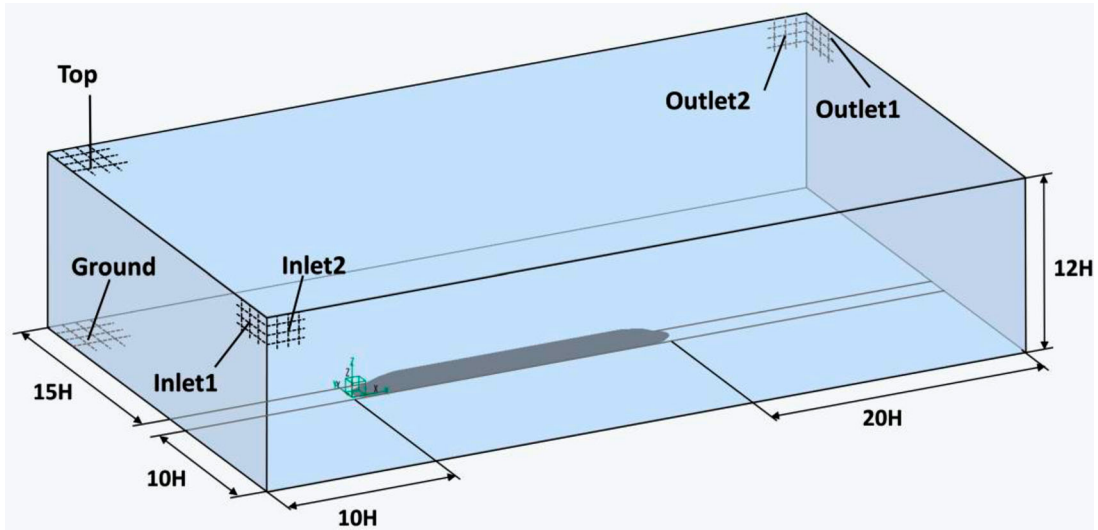


Figure 2. The simulation model's computational domain.

The hexahedral-dominated grids for flow simulation are constructed using the trimmer grid module of the commercial software STAR-CCM+. To accurately predict flow separation around the train, three refinement boxes, namely Box1, Box2, and Box3, are developed. Box1 is employed to cover the flow field underneath the train model using the minimum-sized grid. Box2 refines the meshes around the train and its wake, with the grid size matching that of the train's surface mesh. The third refinement box, Box3, represents the transition region between Box2 and the far-field area. The grid size increases accordingly from Box1 to Box3. Furthermore, a seven-layer prism layer mesh is constructed on the train's surface and the ground to capture the near-wall flow structures. The standard wall functions are utilised, with the first cell's height set at 0.4mm, corresponding to a y^+ value of approximately 40 for the simulated cases. This value is within the y^+ range of 30–300 required by the standard wall function. Mesh refinement scheme and prism layer grids are shown in Figure 3. The total amount of computing grids is approximately 17.35 million.

2.3. Numerical algorithms

In this paper, all computational fluid dynamics analyses are conducted using the commercially available software STAR-CCM+ 9.06. The train moves with train velocity: $u_{train} = 83.33\text{m/s}$, and the crosswind speed v_{wind} variation is set within the range of [17, 23] m/s. The maximum resultant velocity is 86.45m/s, corresponding to a Mach number of 0.254, so the air compressibility can be neglected. Therefore, the governing equations are the incompressible Navier-Stokes equations, which are discretised by the method of finite volume in CFD

simulations. The Semi-Implicit Method for Pressure-Linked Equation (SIMPLE) technique is employed to couple the pressure and velocity fields. And the second-order upwind scheme is adopted for spatial discretization.

The Reynolds-averaged Navier-Stokes (RANS) equations, commonly adopted for streamlined vehicles at small yaw angles (Baker et al., 2009), are used in this study. The shear-stress transport (SST) $k-\omega$ model is selected as the turbulence model, and the k and ω are solved by the second-order upwind scheme. Li et al. (2019) study the performance of different turbulence models in the numerical simulation of trains in crosswind. Comparing the wind tunnel experimental data and numerical results, the SST $k-\omega$ model is considered to be the most accurate model for the aerodynamic prediction of trains. In recent years, the SST $k-\omega$ model has been widely used in the field of high-speed trains and its validity has been proven (Xia et al., 2020; Zhang et al., 2022).

To facilitate analysis, define the aerodynamic coefficient and moment coefficient as follows:

Drag coefficient C_D :

$$C_D = \frac{2F_x}{\rho V^2 S_x} \quad (1)$$

Lift coefficient C_L :

$$C_L = \frac{2F_z}{\rho V^2 S_x} \quad (2)$$

Side force coefficient C_S :

$$C_S = \frac{2F_y}{\rho V^2 S_x} \quad (3)$$

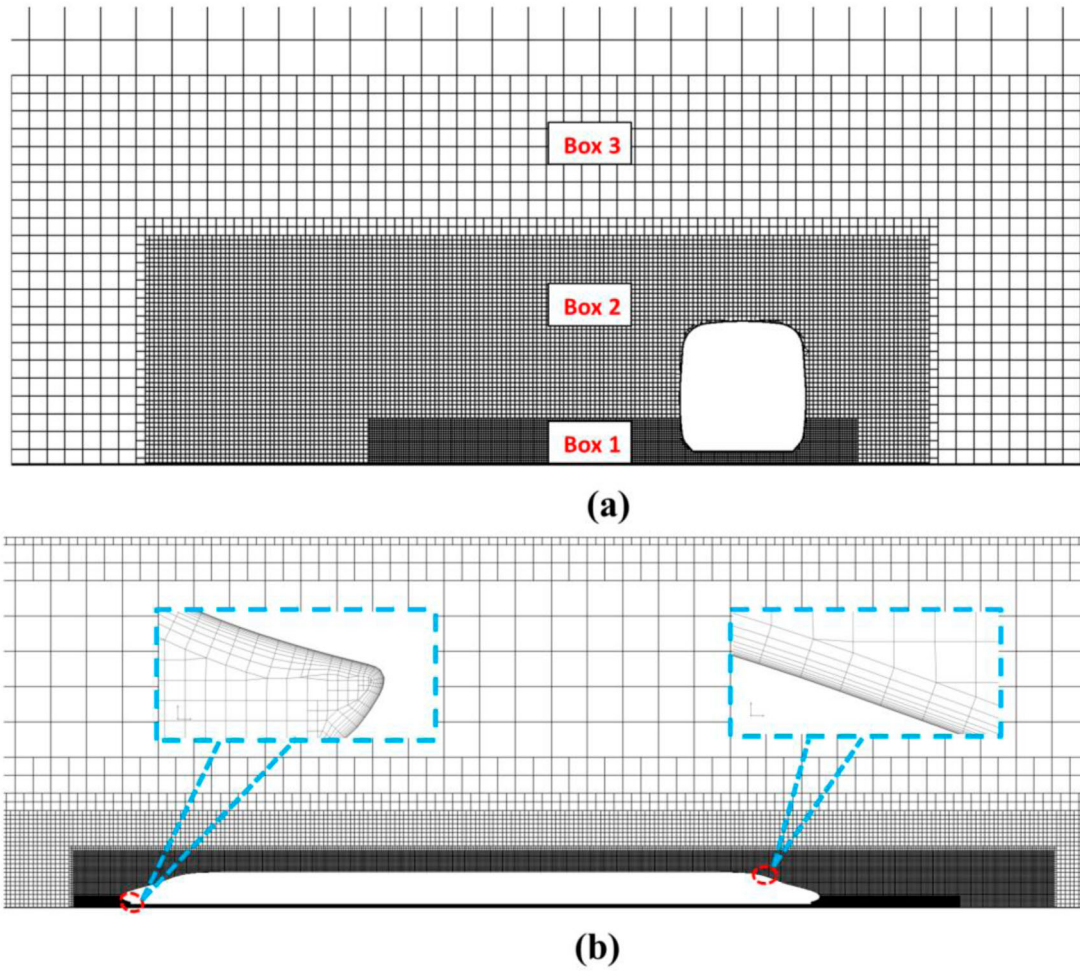


Figure 3. The distribution of grids. (a) side view; (b) front view

Rolling moment coefficient C_M :

$$C_M = \frac{M_x}{0.5\rho V^2 S_x H} \quad (4)$$

In the formula, F_x is the aerodynamic drag of the train, M_x is the rolling moment of the train. ρ is the air density, taken as $1.225\text{kg}/\text{m}^3$; V is the incoming flow velocity, taken as $300\text{km}/\text{h}$; S_x is the reference area, which is the maximum cross-sectional area of the train model, taken as 11.12m^2 . The characteristic length H is 3.8m .

2.4. Numerical validation

To validate the numerical algorithms employed in this study, a comparison between the numerical simulation and wind tunnel test is performed under a 8.77° yaw angle condition. As depicted in Figure 4(a), the wind tunnel test model is a 1:8 scaled model, inclusive of bogies and windshields. The model consists of a leading car, a middle car and a trailing car, with a total length of approximately 10m . The test was conducted in a closed wind tunnel at the China Aerodynamic Research and Development

Centre. The test section of the wind tunnel is 8m wide, 6m high and 15m long. With the installation of a special floor for train tests, the height of the test section is 4.94m and the effective cross-sectional area is 39.2m^2 . The cross-sectional area of the train model is less than 0.25m^2 , so the blockage ratio is less than 1% , where the interference from the cave wall could be negligible. Three cassette-type six-component strain balances were selected for the test to measure the forces and moments of the head, middle and tail cars. The balances were firmly mounted in the inner the model and rigidly fixed to the test floor by stanchions. The domain and boundary conditions in CFD are kept identical to that of the experimental setup. The mesh distribution for the CFD calculation along the longitudinal section and in the boundary layer is shown in Figure 4(b), with a meshing strategy similar to that described previously. In addition, the mesh in the region of bogies and connecting parts is refined, with the total number of grids being approximately 21.7 million. The numerical methodology adopted is in accordance with that described in Section 2.3.

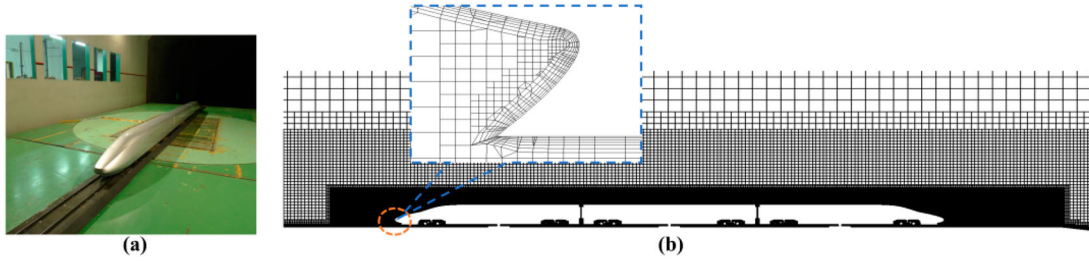


Figure 4. CFD validation. (a) wind tunnel test model, (b) numerical calculation meshing.

Table 1. Comparison of RANS calculation results with wind tunnel test data.

	Experiment	CFD	Error
Total C_D	0.4149	0.4277	1.28%
Head car C_L	0.4701	0.4534	3.55%
Head car C_S	0.6973	0.7131	2.27%
Head car C_M	0.0441	0.0452	2.49%
Middle car C_L	0.4924	0.4867	1.16%
Middle car C_S	0.2293	0.2196	4.23%
Middle car C_M	0.0159	0.0156	1.89%
Tail car C_L	0.3524	0.3425	2.81%
Tail car C_S	0.045	0.0441	2.00%
Tail car C_M	0.0118	0.0115	2.54%

A comparison of aerodynamic force and rolling moment coefficients of each car from the wind tunnel experiments and numerical simulations is presented in Table 1. The errors of all the aerodynamic loads are within 5%, and the errors of the rolling moment coefficients are with 3%, indicating that the numerical algorithms and the mesh configuration are sufficiently precise for aerodynamic design of high-speed trains under crosswind conditions.

3. Robust optimisation process

In the present paper, the process of robust optimisation design is proposed, as shown in Figure 5, which comprises three primary components: parametric modelling, uncertainty analysis, and multi-objective optimisation. The key steps are summarised as follows:

- (1) **Environmental Uncertainty:** The wind speed of the crosswind is defined as the source of uncertainty, and the crosswind speed v_{wind} variation interval is set to [17, 23] m/s.
- (2) **Determining the Deformation Area:** The aerodynamic performance of baseline geometry is evaluated under varying crosswind speeds, and the Non-Intrusive Polynomial Chaos method is used to obtain the variance of the pressure distribution on the train surface, which facilitates the determination of deformation areas.
- (3) **Parametric Shape:** The Local shape function (LSF) method is utilised to parameterise the shape based on the baseline geometry, corresponding to the deformation area.
- (4) **Initial Sampling Points:** The Uniform Latin hypercube method is adopted to generate 30 initial sample points used to calculate the CFD response.
- (5) **Uncertainty Analysis:** The cross-validated Kriging surrogate model is developed using the calculated sample points to predict the aerodynamic response in the uncertainty analysis. Then, The Monte Carlo simulation method is used to obtain the mean and variance of the rolling moment in crosswind conditions.
- (6) **Multi-Objective Optimisation:** The mean and variance of the rolling moment of the leading car are chosen as the optimisation objectives. With appropriate constraints, the Pareto solutions are identified using Non-dominated Sorting Genetic Algorithm-II (NSGA-II).
- (7) **Optimal Design:** The accuracy of the surrogate model can be improved by increasing the number of training sample points. The optimal design is achieved when the surrogate model reaches the desired accuracy and the optimisation converges.

The proposed robust optimisation design method provides a convenient approach for optimising the aerodynamic performance of trains under crosswind conditions, taking into account environmental uncertainties.

3.1. Uncertainty analysis

In order to achieve robust optimisation, it is imperative to consider sources of environmental uncertainty. In aerodynamic shape optimisation, sources of uncertainty can typically be divided into flow conditions and geometric errors. However, since geometric manufacturing errors are comparatively negligible in high-speed trains, this study only considers the effect of uncertain flow conditions. Even a small change in crosswind velocity may affect the flow separation around the

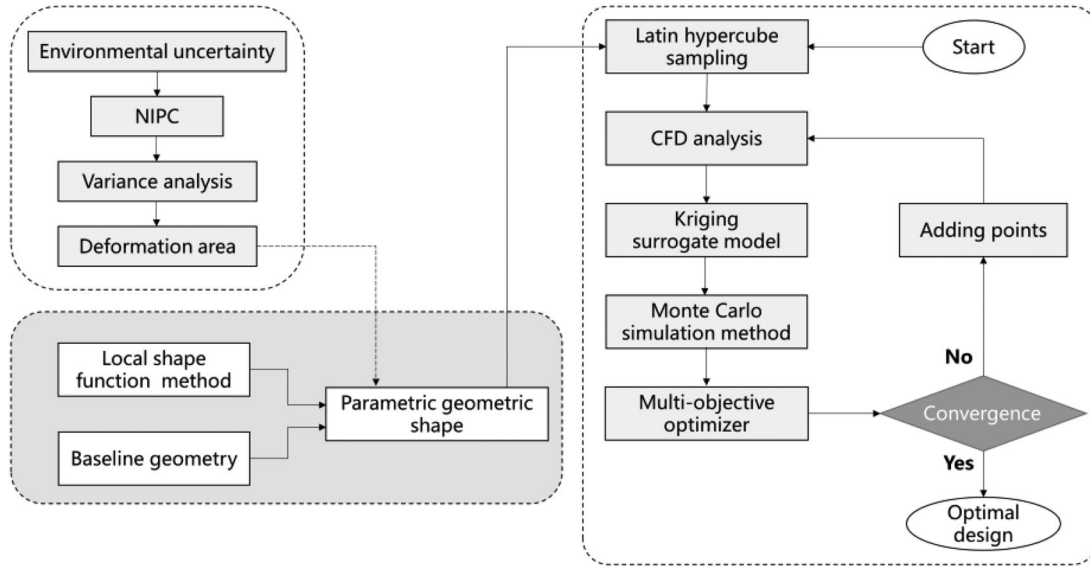


Figure 5. Flow chart of optimisation process.

train, thus uncertainty of crosswind is mainly considered in the present study. For the operating speed, $u_{train} = 300\text{km/h}$, the upper limit of the crosswind velocity is 20m/s according to Chinese technical management regulations for railway (China State Railway Group Co., Ltd, 2019). Consequently, the crosswind velocity change interval is set to $[17, 23]$ m/s in the current research to enhance safety.

The uncertainty propagation method is a crucial step in obtaining the statistical properties of the output response. In this study, the Non-Intrusive Polynomial Chaos (NIPC) method (Ghanem & Spanos, 2003) and the Monte Carlo simulation method (Caflich, 1998) have been employed as the uncertainty propagation methods in pre-analysis and optimisation iteration, respectively. The Monte Carlo simulation method is a standard method to obtain the mean and variance, often used to characterise the uncertainty of output response, through repeated tests, as shown in equations (3-4). In the present study, the mean $E(C_M)$ and variance $\sigma^2(C_M)$ of the rolling moment are obtained by the Monte Carlo simulation method in a multi-objective optimisation process, as shown in equations (5-6). The surrogate model calculates the response of n samples obtained by Latin hypercube sampling (Schaefer et al., 2017).

$$E(C_M) = \frac{\sum_{i=1}^n C_M(x_d, x_{u(i)})}{n} \quad (5)$$

$$\sigma^2(C_M) = \frac{\sum_{i=1}^n (C_M(x_d, x_{u(i)}) - E(C_M))^2}{n-1} \quad (6)$$

Uncertainty propagation is also required for determining the deformation area in pre-analysis, where the uncertainty associated with the baseline shape under various

crosswinds is analysed. Due to the vast amount of data required for Monte Carlo simulation in low-dimensional problems, the NIPC method is employed in this step. This method was first proposed by (Wiener, 1938) and can be divided into two types: intrusive and non-intrusive. The non-intrusive method treats the solver as a 'black box' and calculates the statistical characteristics based on the deterministic solution. In the present work, the non-intrusive method is utilised. The fundamental concept of the NIPC is to approximate stochastic processes as a sum of orthogonal polynomials of random variables. $\xi = \{\xi_1(\theta), \xi_2(\theta), \dots, \xi_n(\theta)\}$ represents random variables. $\Psi_k(\xi_i)$ is a set of orthogonal polynomials. Then the response Y of random variable can be approximated by the following chaotic polynomial expansion:

$$Y = \sum_{k=0}^{\infty} a_k \Psi_k(\xi) \approx \sum_{k=0}^{N_{PC}} a_k \Psi_k(\xi) \quad (7)$$

Where, a_k is the chaotic polynomial coefficient to be solved. N_{PC} is the number of polynomial terms in the approximate expression, which can be determined by the following formula:

$$N_{PC} = \frac{(p+n)!}{p!n!} - 1 \quad (8)$$

p is the order of the polynomial; n is the number of random variables. The linear regression method is adopted to solve chaotic polynomial coefficients a_k , which was proposed by (Isukapalli, 1999). With these coefficients,

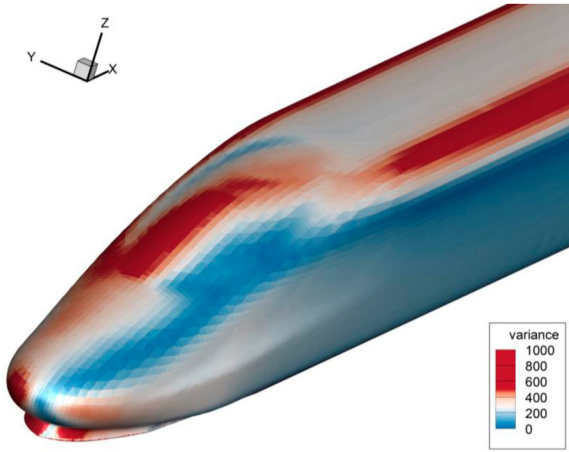


Figure 6. Distribution of variance of surface pressure.

the mean $E(Y)$ and variance $\sigma^2(Y)$ the statistical properties of the output response can be determined.

$$E(Y) = a_0 \quad (9)$$

$$\sigma^2(Y) = \sum_{k=1}^{N_{PC}} a_k^2 E(\Psi_k^2) \quad (10)$$

3.2. Parametric modelling

The objective of the robust design is to enhance the crosswind stability of high-speed trains while minimizing their sensitivity to crosswind velocity. Thus, prior to the parametric modelling, a pre-analysis is necessary to determine the deformation area. This is achieved by selecting 20 crosswind velocity in the range [17, 23] m/s using Latin hypercube sampling and calculating the train surface pressure. The NIPC method is then used to estimate the variance of the surface pressure under different crosswind conditions. The variance distribution of surface pressure on the leading car is presented in Figure 6. The regions with significant variances of pressure distribution indicate higher sensitivity to crosswind velocity. Notably, the variance of the region where flow separation occurs is substantial. As such, the deformation of areas such as the cowcatcher, nose tip, and driver's cab, which exhibit large variances, is crucial in robust optimisation design.

The method of parametric modelling is of great significance for optimisation. Cui et al. (2012) proposed the LSF method and applied it to the design of high-speed trains. In the present study, the LSF method is utilised to parameterise the streamlined shape. This method divides the geometric shape into several deformation regions that are then discretised into grid points. The deformation of each grid point corresponds to the displacement of control points by the shape functions, which are

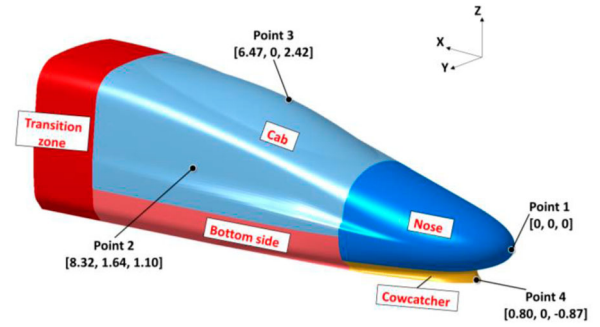


Figure 7. Deformation area division and control point.

Table 2. Range of design variables.

design variable	minimum value/mm	maximum value/mm
$W1$	-840	360
$W2$	-180	120
$W3$	-360	0
$W4$	-120	48
$W5$	-720	120

trigonometric functions that ensures a smooth surface. According to the coordinates of all grid points, the deformation surface can be fitted precisely. A more detailed description of the LSF method can be found in previous study (Yao et al., 2012).

In this case, the nose shape is divided into five deformation regions, as shown in Figure 7. Using Point1 as the origin of the axis, the exact positions of each control points have been presented in the figure, where the unit is metres. Point1 is located on the nose tip, and two design parameters, $W1$ and $W2$, are extracted to control the nose's length and height, respectively. In addition, Point2 relates to the cab, the bottom side, and the transition zone, which controls the body width. The spanwise displacement of Point2 represents the third design parameter, $W3$. Furthermore, the driver's room is controlled by Point3, and its normal displacement is the fourth design parameter, $W4$. Point4 controls the shape of the cowcatcher, and its streamwise displacement is the fifth design parameter, $W5$. It is important to specify the sign of these design variables, where a positive $W1$ means the nose tip becomes shorter, a positive $W2$ means the nose tip becomes higher, a positive $W3$ represents a wider body, a positive $W4$ results in a higher cab, and a negative $W5$ leads to a more prominent cowcatcher. The ranges of these design variables, considering the engineering limitation, are presented in Table 2.

3.3. Construction of surrogate model

Compared with traditional deterministic optimisation, a key feature of robust optimisation is the analysis of uncertainty in each calculation of sample points. Consequently,

the computational cost of robust optimisation is typically higher. For robust aerodynamic optimisation, it is not feasible to use CFD to calculate every sample due to its high cost. As a result, the surrogate model, which is a mapping between the target response and the variables, is adopted instead of CFD for uncertainty analysis. The Kriging model, derived from geostatistics (Kriging, 1951), is used as the surrogate model due to its nonlinear fitting ability and error estimation method, which make it widely used in aerodynamic shape optimisation. The Kriging model is defined as follows:

$$y(x^{(i)}) = F^T(x^{(i)})\beta + z(x^{(i)}), (i = 1, \dots, n) \quad (11)$$

n represents the quantity of sampled points, whereas $x^{(i)}$ refers to an individual sample point. The regression coefficient is represented by the symbol β , and $F^T(x^{(i)})$ denotes a deterministic function that furnishes a comprehensive approximation of the design space. In this paper, $F^T(x^{(i)})$ is a constant. $z(x^{(i)})$ is an error of random distribution that provides an approximation of the simulated local deviation. The average value of $z(x^{(i)})$ is zero, and its variance is represented by σ_z^2 , and its covariance matrix is given by:

$$\begin{aligned} \text{cov}[z(x^{(i)}), z(x^{(j)})] \\ = \sigma_z^2 [R(\theta, x^{(i)}, x^{(j)})], (i, j = 1, \dots, n_s) \end{aligned} \quad (12)$$

n_s is the number of training sample points, and $R(\theta, x^{(i)}, x^{(j)})$ is the correlation function with parameter θ , indicating the spatial correlation between training sample points. Gaussian function is commonly used as the correlation function, and its expression is.

$$\begin{aligned} R(\theta, x^{(i)}, x^{(j)}) = \exp \left[- \sum_{k=1}^m \theta_k |x_k^{(i)} - x_k^{(j)}|^2 \right], \\ (i, j = 1, \dots, n_s) \end{aligned} \quad (13)$$

Where, m is the number of design variables, and $x_k^{(i)}$ is the corresponding design variable value of sample point $x^{(i)}$. To enhance the accuracy of the prediction, the Kriging model necessitates the identification of an appropriate θ_k that renders the prediction error's mean value equal to 0, and the mean square deviation of the prediction error smallest. This is represented mathematically as:

$$\begin{aligned} \text{Min } \varphi(\theta_k) = \frac{n}{2} \ln(\sigma_z^2) + \frac{1}{2} \ln(|R|) \\ \text{s.t. } \theta_k > 0 \end{aligned} \quad (14)$$

The values of the Kriging model's parameters can be obtained by implementing various optimisation algorithms. In the current study, the first Kriging model is

created using the initial samples and their aerodynamic response. Subsequently, in each optimisation step, the accuracy of the Kriging model can be enhanced by adding new accurately computed samples, which are selected based on a suitable points-adding criterion.

3.4. Multi-objective optimisation

Robust optimisation is a multi-objective optimisation problem that aims to simultaneously minimise the mean and variance of a given metric. Under uncertain crosswind conditions, robust optimisation is applied to reduce the mean and variance of the rolling moment of the leading car. The optimisation problem can be formulated as follows:

$$\begin{aligned} \text{Min } (E(C_M), \sigma(C_M)) \\ \text{s.t. } x_L \leq x \leq x_U \\ C_M \leq C_M^{\text{CRH380A}} \\ V \geq 97\%V^{\text{CRH380A}} \end{aligned} \quad (15)$$

Where, $E(C_M)$ and $\sigma^2(C_M)$ denote the mean and variance, respectively, of the rolling moment of the leading car when crosswind velocity varies in the range of [17, 23] m/s. The variable vector x includes both the design variables $x_d = \{W1, W2, W3, W4, W5\}$ and the uncertainty variable x_u . The variables are subjected to constraints within a certain range where x_L and x_U are the lower and upper bounds of the design variables respectively. Furthermore, it is required that the rolling moment of the optimised shape C_M be lower than that of the baseline geometry C_M^{CRH380A} . It also ensures that the volume of the leading car V at least 97% greater than the initial profile volume V^{CRH380A} .

To solve this optimisation problem, the current study employs the NSGA-II (Deb et al., 2002) algorithm, a multi-objective genetic algorithm based on the Pareto optimal concept. Because of the need to analysis uncertainty, the surrogate model is required to have high accuracy in both the local and overall design space. To improve the accuracy of the surrogate model, the points-adding criterion, which combines the MSP (Minimising the Surrogate model Prediction) criterion and the MSE (Mean Square Error) criterion, is employed. This method involves adding points near the optimal point and the maximum variance point of the Kriging model in several iterations until the desired accuracy is achieved.

4. Results and discussion

The initial 30 sample points are chosen using Latin hypercube sampling within the range of five parametric design

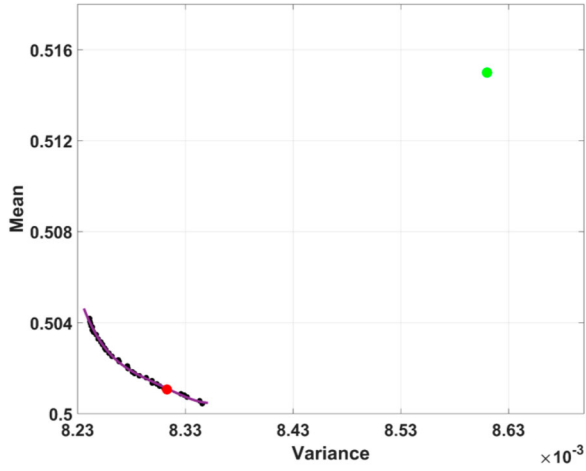


Figure 8. Pareto front resulting from the multi-objective optimisation problem.

variables and the crosswind velocity, and the rolling moment for these points is calculated using CFD to construct the initial Kriging model. Subsequently, six rounds of adding points are performed, for a total of 105, and the optimisation objectives gradually converged towards a narrow region. The Pareto front of this multi-objective optimisation problem, which aims to minimise the mean and variance of the rolling moment C_M , is obtained and shown in Figure 8. The green dot refers to the baseline geometry, and the red dot refers to the robust optimal design chosen from the Pareto front. In addition, a deterministic optimal design is also obtained using traditional optimisation methods for a crosswind speed of 20m/s (the average value of the crosswind speed in the design space). The aerodynamic performance of the baseline geometry, the deterministic optimal shape and the robust optimal shape will be compared in this section.

4.1. Accuracy analysis of the Kriging model

It is necessary to validate the accuracy of the Kriging surrogate model before analysing the optimisation results. The baseline geometry, the deterministic optimal shape and the robust optimal shape are computed for ten random crosswind speeds, v_{wind} , ranging from 17 to 23 m/s. Specifically, the baseline geometry, the deterministic optimal shape, and the robust optimal shape are assessed by calculating their rolling moment coefficient using computational fluid dynamics. In addition to the CFD results, the predicted rolling moment coefficient obtained from the Kriging model for each of these 30 scenarios is also recorded. The comparison of CFD and Kriging predictions is depicted in Figure 9 (a) (b) (c).

The surrogate model's predictions for the three shapes at various wind speeds are in excellent agreement with

the CFD calculations. Additionally, Figure 9 (d) displays the relative prediction error distribution. The maximum relative prediction error is less than 0.7%, indicating that the Kriging model can accurately represent the mapping between the input variables and aerodynamic forces. To further assess the accuracy of the surrogate model, the root mean square error (RMSE) is introduced as a metric for quantifying the prediction error.

$$RMSE = \sqrt{\frac{1}{m} \sum_{i=1}^m (f(x_i) - y_i)^2} \quad (16)$$

Where, $f(x_i)$ is the Kriging model's predictions; y_i is the rolling moment of the leading car calculated by high-fidelity CFD. m is the number of samples, which is 10. $RMSE$ for these three shapes is shown in Table 3. The $RMSE$ of the Kriging model is less than 0.01, indicating the model is constructed with high accuracy. Overall, the validation results demonstrate that the Kriging model is sufficiently accurate to provide reliable predictions.

4.2. Optimisation results

Table 4 displays the exact values of the design variables for the baseline geometry, the deterministic optimal shape, and the robust optimal shape. In addition, Figure 10 presents a visual comparison of these three designs, where the baseline geometry is depicted in blue, the deterministic optimal shape in purple, and the robust optimal shape in yellow. It can be seen that the optimised shapes exhibit significant changes, particularly in the nose tip, driver's cab, and the cowcatcher area. Specifically, the optimised nose tips are shorter and lower than the baseline geometry, resulting in a more streamlined and aerodynamic shape. The driver's cab has also been slightly reduced in height, further contributing to the overall improved aerodynamic performance. Interestingly, although the shapes of the two optimised designs are quite similar, there are noticeable differences in the cowcatcher area. In particular, the cowcatcher of the deterministic optimal shape is longer than that of the robust optimal shape. This difference depends on whether uncertainty is taken into account in the optimisation process.

When the train operates at $u_{train} = 300$ km/h under crosswind in the range of [17, 23] m/s, Table 5 displays the mean $E(C_M)$ and variance $\sigma^2(C_M)$ of the rolling moment coefficient of the leading car. Specifically, the rolling moment coefficient under 20 m/s crosswind is presented in the Table 5. The mean and variance of both the robust optimal shape and deterministic optimal shape are substantially lower than those of the baseline geometry. The robust optimal shape, in particular, exhibits the

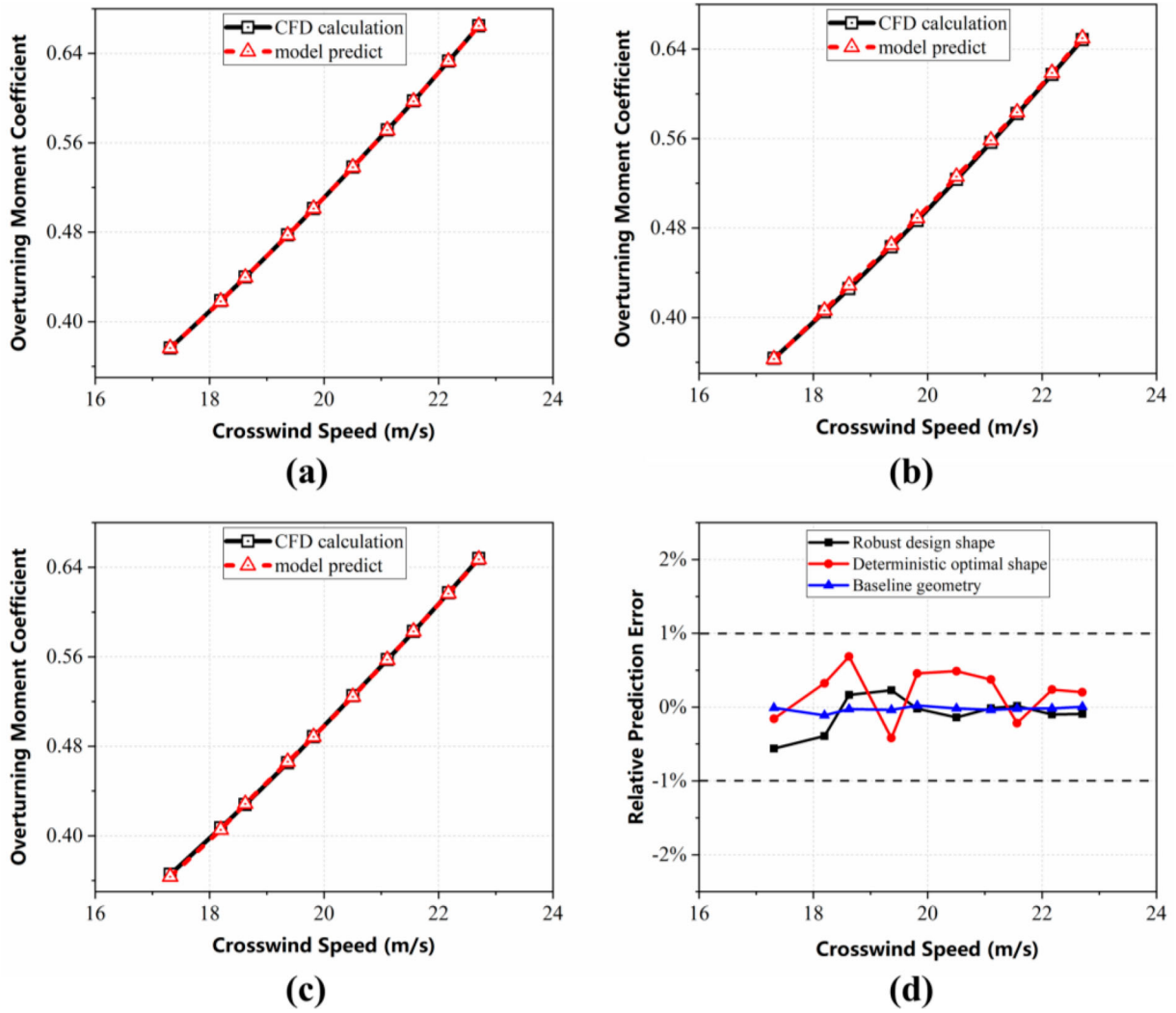


Figure 9. Comparison of model predictions and CFD calculations for test sample points and prediction error distribution. (a) baseline geometry, (b) deterministic optimal shape, (c) robust optimal shape, (d) distribution of the relative prediction error.

Table 3. Comparison of RMSE.

Design scheme	RMSE
Baseline geometry	0.0009
Deterministic optimal shape	0.0045
Robust optimal shape	0.0032

lowest values. These findings suggest that the aerodynamic performance of the robust optimal shape is less sensitive to the changes in crosswind speed due to its lower variance. Compared to the baseline geometry, the robust optimal shape reduces the mean and variance values by 2.26% and 3.37%, respectively. Moreover, $C_M^{20m/s}$ indicates the rolling moment coefficient under the 20m/s crosswind. The rolling moment coefficient under the 20m/s of the robust optimal train is 2.45% lower than that of the baseline geometry. Given the streamlined and aerodynamically superior design of the prototype train, this reduction in rolling moment is a significant achievement.

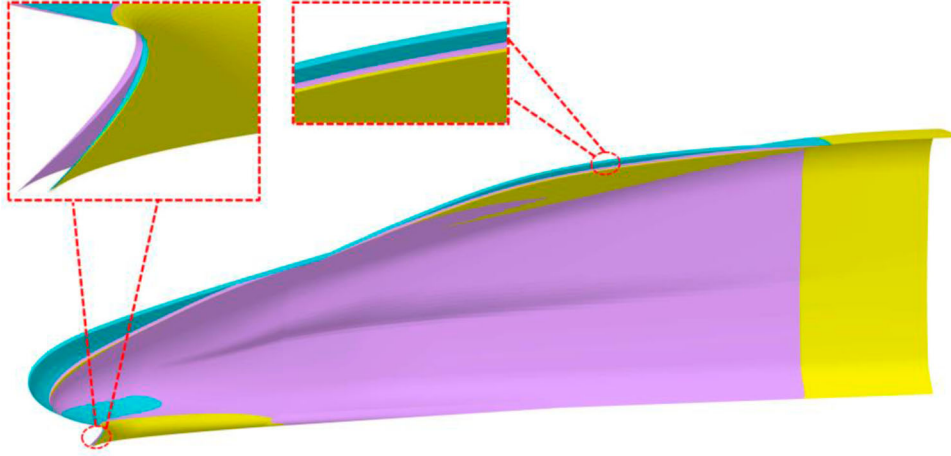
To compare the aerodynamic performance more conveniently, the reduction of rolling moment RM is defined as the ratio of the change in rolling moment before and after optimisation to the rolling moment of the baseline geometry, as expressed in Equation (17):

$$RM = \frac{C_M^{opt} - C_M^{base}}{C_M^{base}} \times 100\% \quad (17)$$

Where, C_M^{opt} represents the rolling moment coefficient of the deterministic optimisation or the robust optimisation, while C_M^{base} is the rolling moment coefficient of the baseline geometry. Figure 11 displays the distribution of RM when the crosswind velocity ranges from 17 to 23 m/s. While the deterministic optimisation performs better at a crosswind speed of 20 m/s, the robust optimisation exhibits superior performance across the entire range of crosswind. These comparisons

Table 4. Comparison of design parameters.

Design scheme	W1/mm	W2/mm	W3/mm	W4/mm	W5/mm
Baseline geometry	0	0	0	0	0
Deterministic optimal shape	357	-165	-75	-85	62
Robust optimal shape	359	-172	-39	-98	-4

**Figure 10.** Shape comparison before and after optimisation.**Table 5.** Comparison of rolling moment before and after optimisation.

Design scheme	$E(C_M)$	$\sigma^2(C_M)$	$C_M^{20m/s}$
Baseline geometry	0.515	0.00861	0.511
Deterministic optimal shape	0.502	0.00849	0.496
Robust optimal shape	0.501	0.00831	0.498

of the aerodynamic force exhibit the superiority of robust optimisation.

4.3. Analysis of flow field

When the train operates under crosswind conditions, the unsteady characteristics of the flow field around the train become apparent. To explore the reasonableness of the optimisation result in detail, the Improved Delayed Detached-Eddy Simulation (IDDES) method based on the $k-\omega$ SST two-equation model is used to analyse the difference of flow field between the baseline geometry and the robust optimal shape. IDDES has been frequently used to analyse the aerodynamic performance of trains due to its well-known performance for separate flow predictions (Wang et al., 2021). The SIMPLE technique is employed to couple the pressure and velocity fields. The convective term is discretised using a hybrid scheme where the RANS regions use the second-order upwind scheme and the LES regions use the bounded central differentiation. A second-order implicit scheme was employed for the time progression. The unsteady calculation method accompanying the dual-time step format was used for time discretization.

The number of internal iteration steps is 15 to ensure that the residual value decreases by at least 1 order of magnitude within each time step. Set feature time $T_{ref} = H/u_{train}$, and the physical time step is set to $\Delta t = 1 \times 10^{-4} s \approx 0.002 T_{ref}$, which is sufficient to capture not only the main flow structures, but also details such as detachment and vortex formation. The computational domain and boundary conditions are the same as before, but with finer grids of approximately 90 million in amount. The baseline geometry and the robust optimal shape is recalculated by the IDDES. The rolling moments and side forces under a crosswind of 20m/s obtained from the RANS and the IDDES are compared, as shown in the Table 6. The upper right corner marker indicates a crosswind wind speed of 20m/s. Minor differences were found in the magnitude of the aerodynamic forces obtained by the two calculation methods, but the trend of improvement before and after optimisation was consistent.

First, a comparison is made between the surface pressure distributions, which directly determine the aerodynamic force differences, of the baseline geometry and the robust optimal shape. Figure 12 displays the time-average pressure distribution of these two shapes, which exhibit some similarities before and after optimisation. On the windward side, the nose of the train has a significant area of positive pressure. On the leeward side, there is an enormous negative pressure area, most noticeable near the driver's cab. The immense pressure difference between the windward and leeward sides is the main cause of the rolling moment. Compared to the baseline geometry, the

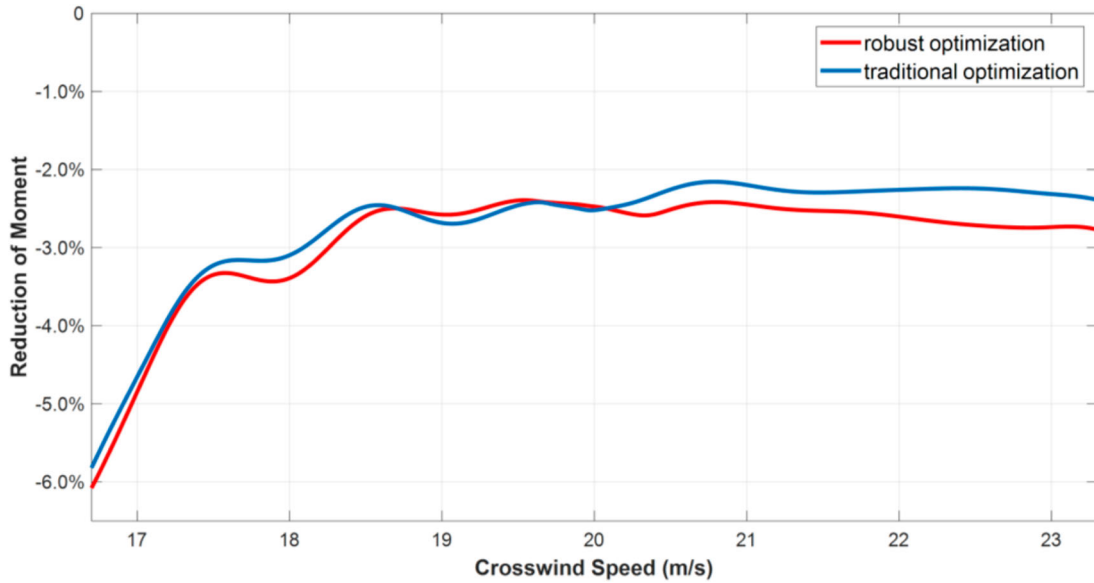


Figure 11. Distribution of RM.

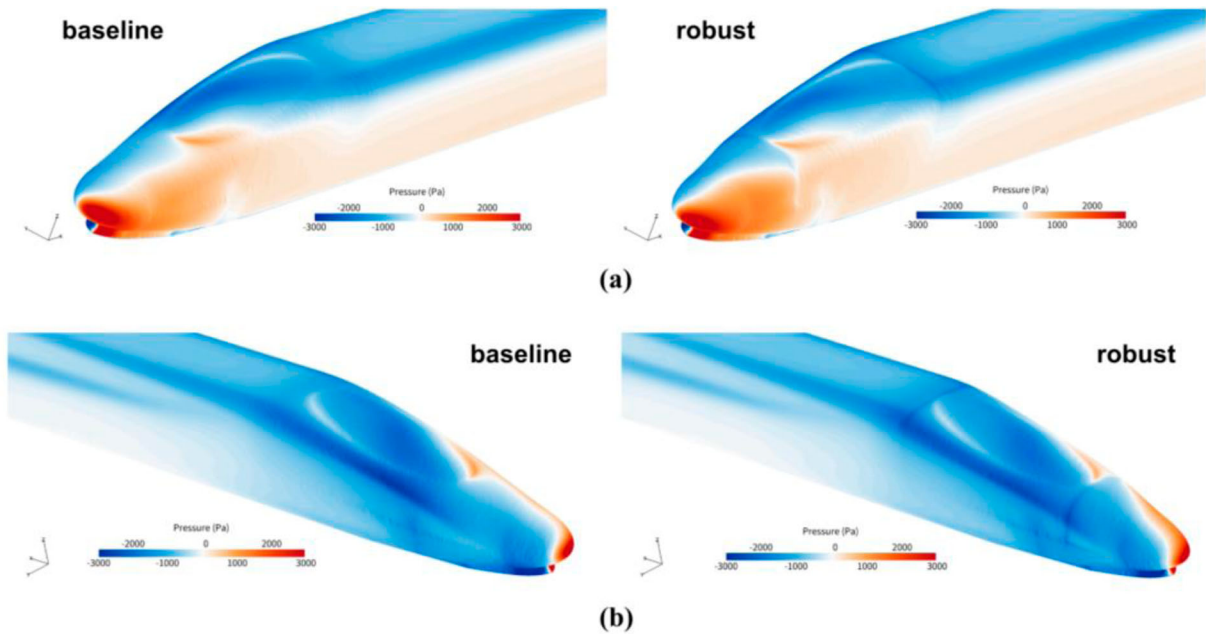


Figure 12. Time-average surface pressure distribution at the nose of the train. (a) windward; (b) leeward.

transition from positive to negative pressure on the nose of the robust optimal shape is smoother. This optimised shape can suppress flow separation and, as a result, reduce the rolling moment. In contrast, the area of negative pressure near the driver's cab of the optimised shape is less

prominent on the leeward side than it is in the baseline geometry.

Figure 13 illustrates the difference in time-average velocity contours along the longitudinal section of the train. The flow field forms a stagnation point at the front

Table 6. Comparison of rolling moment and side force of head car calculated by IDDES and RANS.

	$C_M^{20m/s}$ (IDDES)	$C_M^{20m/s}$ (RANS)	$C_S^{20m/s}$ (IDDES)	$C_S^{20m/s}$ (RANS)
Baseline geometry	0.527	0.511	1.112	1.069
Robust optimal shape	0.511	0.496	1.108	1.066
Reduction	3.03%	2.93%	0.36%	0.28%

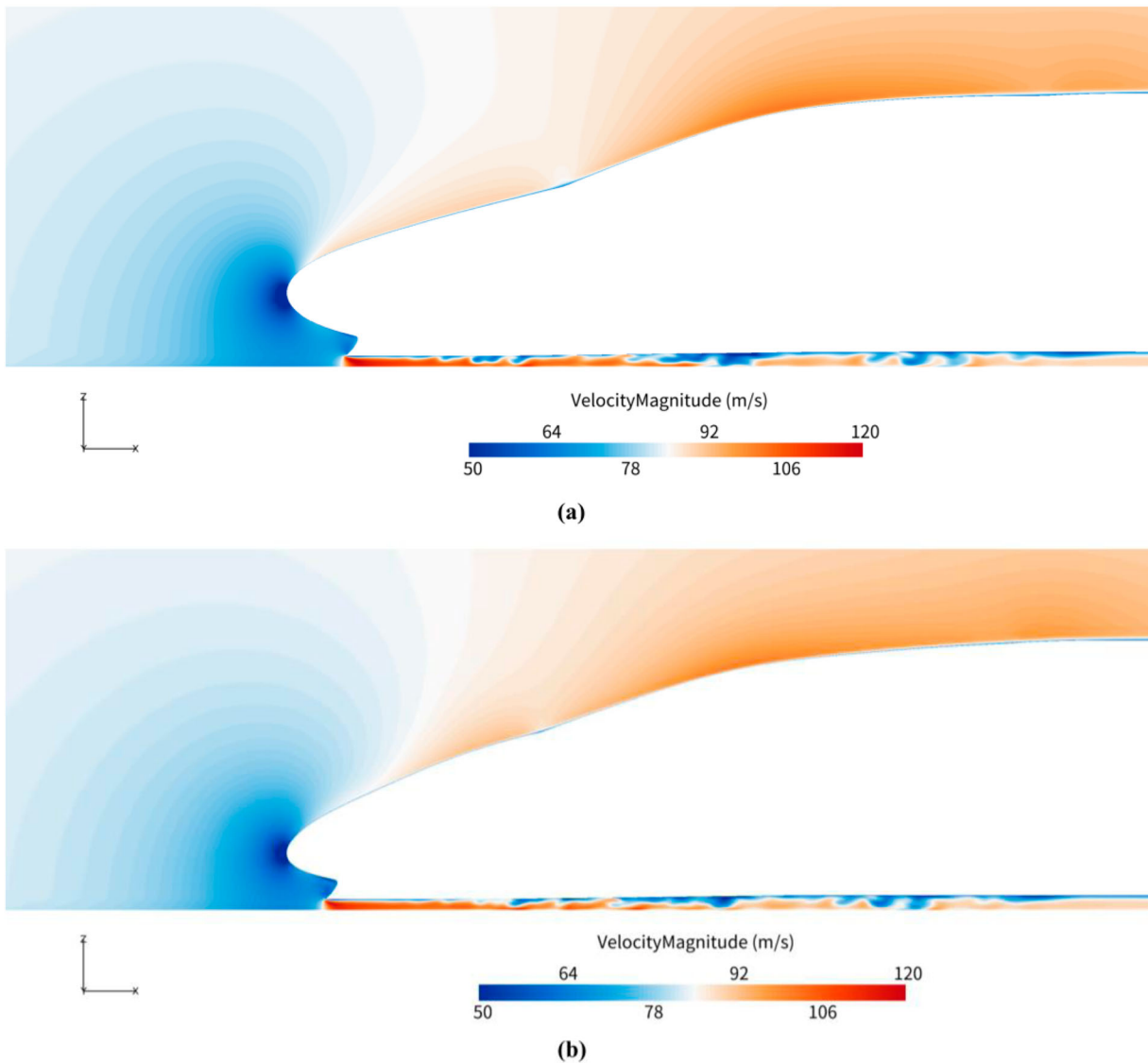


Figure 13. Time-average velocity contours on longitudinal section. (a)baseline geometry; (b)robust optimal shape.

of the nose tip where the pressure is high, and the pressure gradually decreases as the airflow speed increases along the streamline. Due to the large curvature of the driver's cab, the airflow further speeds up, leading to the formation of a negative pressure area. The optimised airflow accelerates more smoothly from front to back compared to the baseline geometry. Moreover, the velocity at the driver's cab is also lower in the optimised flow field. It can be deduced that the optimisation makes the velocity change much smoother, resulting in a more uniform pressure distribution on the surface.

Figure 14 displays the instantaneous iso-surfaces of the Q criterion shaded by pressure for both the baseline geometry and the robust optimal shape. The vortices observed in both cases are similar, with three main vortices present, named V1, V2 and V3 respectively. V1 arises from the separation the nose cone and the

streamlined region, and has the most significant impact on the rolling moment coefficient of the head car. V2 is created on the roof of the middle car while V3 arises from the separation of the trail car. V1 is most influenced by the streamlined shape of the head car. Compared to the baseline geometry, V1 in the optimised flow field is significantly weaker than that in the initial flow field. Thus, V1 carries less energy and is more easily dissipated because of the small scale after optimisation. Due to the weakness of vortex structures on the leeward side, the rolling moment induced by vortex shedding is reduced.

5. Conclusions

Current study presents an innovative approach to the aerodynamic robust optimisation of high-speed trains, with the aim of enhancing their stability and reducing

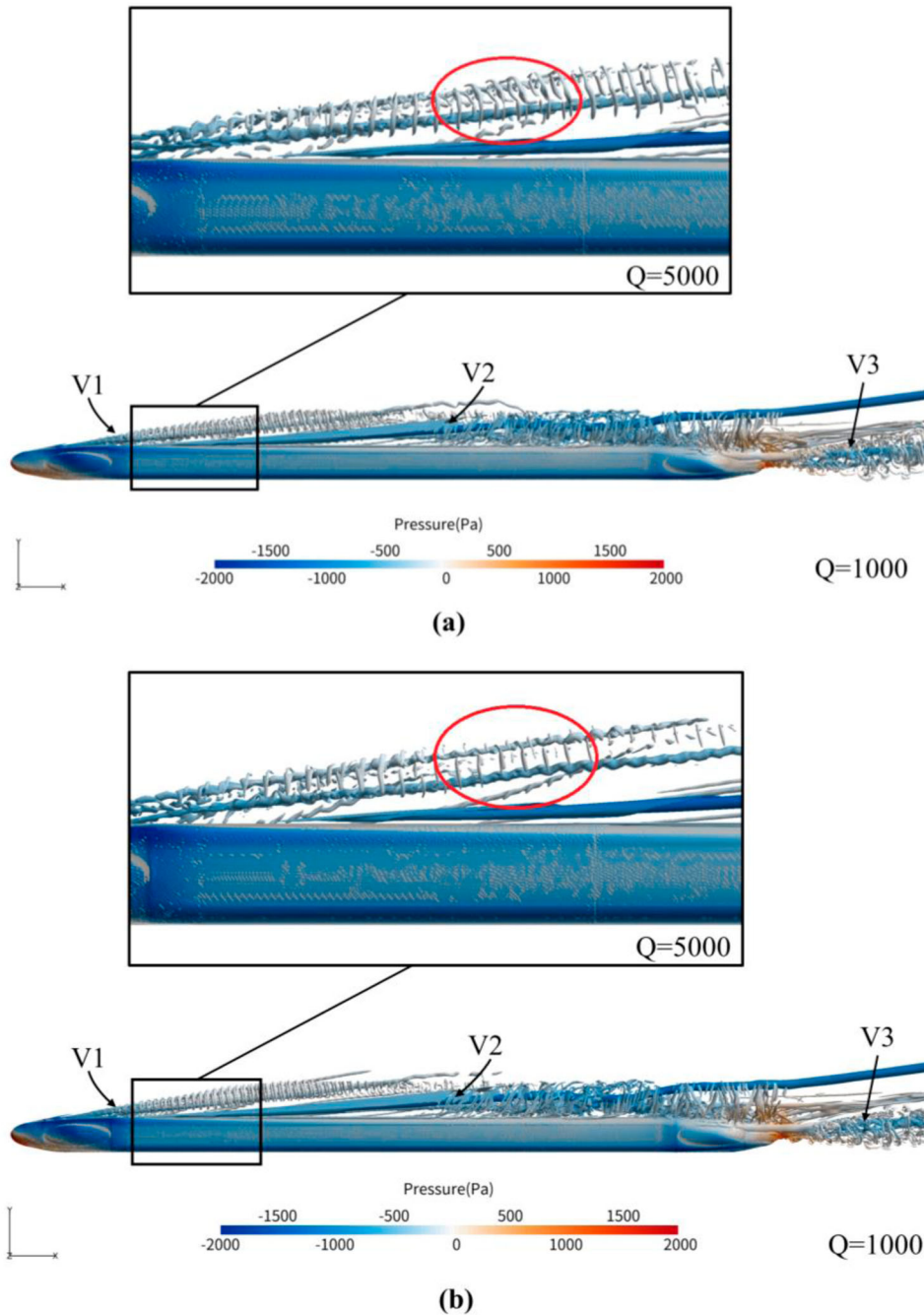


Figure 14. The instantaneous iso-surfaces of Q criterion at 5000. (a)baseline geometry; (b)robust optimal shape.

their sensitivity to crosswind variations. The following highlights the methods and conclusions of this study:

- (1) Environmental uncertainty is taken into consideration during the optimisation process, with crosswind speeds, v_{wind} , ranging from 17 m/s to 23 m/s. The Non-Intrusive Polynomial Chaos method is utilised to analyse the variance of surface pressure, which helped in determining the deformation area. Furthermore, a parametric model of the train is developed using the LSF method, which can control the shape deformation of the cowcatcher, driver's room, nose tip, and cross-section.
- (2) The Monte Carlo simulation method and Kriging surrogate model are elaborately combined to create an efficient uncertainty propagation method for high-speed trains, which is then integrated with NSGA-II to establish an aerodynamic robust optimisation framework. This framework enables efficient robust design of the aerodynamic shape of high-speed trains.

- (3) After optimisation, the aerodynamic performance of the train under uncertain crosswind velocities is significantly improved. Specifically, the robust optimisation reduces the mean and variance of train rolling moment by 2.26% and 3.37%, respectively, compared to the baseline geometry. Additionally, the aerodynamic performance of the robust optimal train is better than that of the deterministic optimal train across the entire range of crosswind speeds.
- (4) Robust optimisation not only improves the aerodynamic performance of high-speed trains but also reduces their sensitivity to crosswind variations. By adopting this framework, high-speed trains can achieve higher levels of security.

Overall, current study offers an innovative and efficient approach to achieve aerodynamically robust optimisation of high-speed trains. It can be applied into practical applications to promote safe and reliable operation of these vehicles.

Acknowledgements

The numerical calculations in this study were carried out on the ORISE Supercomputer.

Disclosure statement

No potential conflict of interest was reported by the author(s).

Funding

This work is supported by the China National Railway Group Science and Technology Program grant (N2022T001, P2021J036).

References

- Andersson, E., Häggström, J., Sima, M., & Stichel, S. (2004). Assessment of train-overturning risk due to strong crosswinds. *Proceedings of the Institution of Mechanical Engineers, Part F: Journal of Rail and Rapid Transit*, 218(3), 213–223. <https://doi.org/10.1243/0954409042389382>
- Baker, C., Cheli, F., Orellano, A., Paradot, N., Proppe, C., & Rocchi, D. (2009). Cross-wind effects on road and rail vehicles. *Vehicle System Dynamics*, 47(8), 983–1022. <https://doi.org/10.1080/00423110903078794>
- Cafilisch, R. E. (1998). Monte Carlo and quasi-Monte Carlo methods. *Acta Numerica*, 7, 1–49. <https://doi.org/10.1017/S0962492900002804>
- Cheli, F., Ripamonti, F., Rocchi, D., & Tomasini, G. (2010). Aerodynamic behaviour investigation of the new EMUV250 train to cross wind. *Journal of Wind Engineering and Industrial Aerodynamics*, 98(4), 189–201. <https://doi.org/10.1016/j.jweia.2009.10.015>
- China State Railway Group Co., Ltd, C. S. R. G. Co., Ltd. (2019). *Technical management regulations for railway (high speed railway)*. China Railway Publishing House.. <https://pdc.capub.cn/search.html#/detail?id=qp4cbgs2qmvowqz4nw54hbwhujgwuk4c2xxltf5peag2k4oqhyda&from=1&type=marc>
- Cui, K., Wang, X. P., Hu, S. C., Gao, T. Y., & Yang, G. (2012). Shape optimization of high-speed train with the speed of 500kph. In Y.-Q. Ni, & X.-W. Ye (Eds.), *Proceedings of the 1st international workshop on high-speed and intercity railways* (pp. 187–197). Springer.
- Deb, K., Pratap, A., Agarwal, S., & Meyarivan, T. (2002). A fast and elitist multiobjective genetic algorithm: NSGA-II. *IEEE Transactions on Evolutionary Computation*, 6(2), 182–197. <https://doi.org/10.1109/4235.996017>
- Ghanem, R., & Spanos, P. D. (2003). *Stochastic finite elements: A spectral approach* (Rev. ed). Dover Publications.
- Huo, X.-S., Liu, T.-H., Chen, Z.-W., Li, W.-H., Niu, J.-Q., & Gao, H.-R. (2023). Aerodynamic characteristics of double-connected train groups composed of different kinds of high-speed trains under crosswinds: A comparison study. *Alexandria Engineering Journal*, 64, 465–481. <https://doi.org/10.1016/j.aej.2022.09.011>
- Isukapalli, S. S. (1999). *Uncertainty analysis of transport-transformation models*. Rutgers The State University of New Jersey, School of Graduate Studies.
- Krajnovic, S., Helgason, E., & Hafsteinsson, H. (2012). *Proceedings of the first international conference on railway technology: Research, development and maintenance*. Civil-Comp Press. Paper 162.
- Krige, D. G. (1951). *A statistical approach to some mine valuation and allied problems on the Witwatersrand* (M.Sc. thesis). University of Witwatersrand, Johannesburg.
- Li, T., Qin, D., & Zhang, J. (2019). Effect of RANS turbulence model on aerodynamic behavior of trains in crosswind. *Chinese Journal of Mechanical Engineering*, 32(1), 85. <https://doi.org/10.1186/s10033-019-0402-2>
- Liu, T.-H., Wang, L., Chen, Z.-W., Gao, H.-R., Li, W.-H., Guo, Z., Xia, Y.-T., Huo, X.-S., & Wang, Y.-W. (2022). Study on the pressure pipe length in train aerodynamic tests and its applications in crosswinds. *Journal of Wind Engineering and Industrial Aerodynamics*, 220, 104880. <https://doi.org/10.1016/j.jweia.2021.104880>
- Luckring, J., Hemsch, M., & Morrison, J. (2003). *Uncertainty in computational aerodynamics*. 41st Aerospace Sciences Meeting and Exhibit, Reno, Nevada.
- Montenegro, P. A., Heleno, R., Carvalho, H., Calçada, R., & Baker, C. J. (2020). A comparative study on the running safety of trains subjected to crosswinds simulated with different wind models. *Journal of Wind Engineering and Industrial Aerodynamics*, 207, 104398. <https://doi.org/10.1016/j.jweia.2020.104398>
- Muñoz-Paniagua J., & García J. 2019. Aerodynamic surrogate-based optimization of the nose shape of a high-speed train for crosswind and passing-by scenarios. *Journal of Wind Engineering and Industrial Aerodynamics*, 184, 139–152.
- Park, G.-J., Lee, T.-H., Lee, K. H., & Hwang, K.-H. (2006). Robust design: An overview. *AIAA Journal*, 44(1), 181–191. <https://doi.org/10.2514/1.13639>
- Pelletier, D., Turgeon, E., Lacasse, D., & Borggaard, J. (2003). Adaptivity, sensitivity, and uncertainty: Toward standards of good practice in computational fluid dynamics. *AIAA Journal*, 41(10), 1925–1933. <https://doi.org/10.2514/2.1908>
- Raghunathan, R. S., Kim, H.-D., & Setoguchi, T. (2002). Aerodynamics of high-speed railway train. *Progress in Aerospace*

- Sciences*, 38(6), 469–514. [https://doi.org/10.1016/S0376-0421\(02\)00029-5](https://doi.org/10.1016/S0376-0421(02)00029-5)
- Schaefer, J., Hosder, S., West, T., Rumsey, C., Carlson, J.-R., & Kleb, W. (2017). Uncertainty quantification of turbulence model closure coefficients for transonic wall-bounded flows. *AIAA Journal*, 55(1), 195–213. <https://doi.org/10.2514/1.J054902>
- Tomasini, G., Giappino, S., Cheli, F., & Schito, P. (2016). Wind-breaks for railway lines: Wind tunnel experimental tests. *Proceedings of the Institution of Mechanical Engineers, Part F: Journal of Rail and Rapid Transit*, 230(4), 1270–1282. <https://doi.org/10.1177/0954409715596191>
- Wang, M. Y., Hashmi, S. A., Sun, Z. X., Guo, D. L., Vita, G., Yang, G. W., & Hemida, H. (2021). Effect of surface roughness on the aerodynamics of a high-speed train subjected to crosswinds. *Acta Mechanica Sinica*, 37(7), 1090–1103. <https://doi.org/10.1007/s10409-021-01099-7>
- Wiener, N. (1938). The homogeneous chaos. *American Journal of Mathematics*, 60(4), 897–936. <https://doi.org/10.2307/2371268>
- Xia, Y., Liu, T., Gu, H., Guo, Z., Chen, Z., Li, W., & Li, L. (2020). Aerodynamic effects of the gap spacing between adjacent vehicles on wind tunnel train models. *Engineering Applications of Computational Fluid Mechanics*, 14(1), 835–852. <https://doi.org/10.1080/19942060.2020.1773319>
- Yao, S., Guo, D., Sun, Z., & Yang, G. (2015). A modified multi-objective sorting particle swarm optimization and its application to the design of the nose shape of a high-speed train. *Engineering Applications of Computational Fluid Mechanics*, 9(1), 513–527. <https://doi.org/10.1080/19942060.2015.1061557>
- Yao, S., Guo, D., & Yang, G. (2012). Three-dimensional aerodynamic optimization design of high-speed train nose based on GA-GRNN. *Science China Technological Sciences*, 55(11), 3118–3130. <https://doi.org/10.1007/s11431-012-4934-2>
- Yao, Z., Zhang, N., Chen, X., Zhang, C., Xia, H., & Li, X. (2020). The effect of moving train on the aerodynamic performances of train-bridge system with a crosswind. *Engineering Applications of Computational Fluid Mechanics*, 14(1), 222–235. <https://doi.org/10.1080/19942060.2019.1704886>
- Zhang, J., Adamu, A., Su, X., Guo, Z., & Gao, G. (2022). Effect of simplifying bogie regions on aerodynamic performance of high-speed train. *Journal of Central South University*, 29(5), 1717–1734. <https://doi.org/10.1007/s11771-022-4948-2>